Opto-Electronic Science

CN 51-1800/O4 ISSN (Print) 2097-0382 ISSN (Online) 2097-4000

Interpretable low-dose CT enhancement via multi-Gaussian cluster variance reduction

Xiaofeng Zhang, Yilan Zhu, Yongsheng Huang, Jielong Yang, Zhili Wang, Kai Zhang, Si Chen, Linbo Liu and Xin Ge*

Citation: Zhang XF, Zhu YL, Huang YS et al. Interpretable low-dose CT enhancement via multi-Gaussian cluster variance reduction. *Opto-Electron Sci* **5**, 250042 (2026).

https://doi.org/10.29026/oes.2026.250042

Received: 12 December 2025; Accepted: 21 February 2026; Published online: 25 March 2026

OES | Opto-Electronic Science

Article

March 2026, Vol. 5, No. 3

Open Access

Interpretable low-dose CT enhancement via multi-Gaussian cluster variance reduction

Xiaofeng Zhang[1], Yilan Zhu[1], Yongsheng Huang[1], Jielong Yang[2], Zhili Wang[3], Kai Zhang[4], Si Chen[5], Linbo Liu[6] and Xin Ge[1]*

Abstract: Computed tomography (CT) is indispensable in both clinical medicine and biological research, yet reducing radiation exposure while maintaining image quality remains a big challenge. To address this, we propose multi-Gaussian Cluster Variance Reduction (mGCVR), a method that enables low-dose CT images to approximate the quality of high-dose scans. mGCVR models the heterogeneous tissue CT intensity distribution using multiple Gaussian components, and performs denoising by shrinking the variance within each component. In biological imaging experiments, mGCVR consistently improves image quality across the entire field of view. Compared with classical denoising algorithms, mGCVR produces images that more closely resemble high-dose clinical CT images and achieves superior performance in quantitative metrics. These results validate the effectiveness of mGCVR and highlight its potential for broad use in both medical imaging and scientific applications.

Keywords: X-ray imaging; denoising; histogram-domain processing; image enhancement; low-dose CT

DOI: 10.29026/oes.2026.250042 | CSTR: 32246.14.oes.2026.250042

Citation: Zhang XF, Zhu YL, Huang YS et al. Interpretable low-dose CT enhancement via multi-Gaussian cluster variance reduction. *Opto-Electron Sci* **5**, 250042 (2026).

1 Introduction

In computed tomography (CT) imaging, X-rays traverse materials with different attenuation properties, and the transmitted photons are detected and converted into electrical signals. Reconstruction algorithms are then used to compute the spatial distribution of attenuation coefficients, which are subsequently mapped to grayscale values to generate tomographic cross-sectional images[1]. CT is widely applied in clinical practice, including disease diagnosis[2], trauma assessment and preoperative planning. With continuous technological advancements, approaches such as dual-energy CT[3] and spectral CT now enable material differentiation, virtual monoenergetic imaging[4–6], and other specialized applications[7,8].

Across all CT modalities, there remains a strong demand for achieving diagnostic goals at lower radiation doses. Reduced dose inevitably decreases the number of detected photons, thereby lowering the signal-to-noise ratio. Therefore, post-processing methods that suppress noise and recover diagnostically relevant information buried in low-dose data are of critical importance[9]. In recent years, neural network approaches have achieved remarkable denoising performance[10,11], often surpassing non-learning based algorithms in terms of SNR[12]. Studies have combined convolutional neural networks with noise thresholding strategies to improve low-dose CT performance[13,14]. However, neural networks typically require large, task-specific training datasets for optimal performance, and their limited interpretability raises concerns regarding reliability and authenticity in clinical use.

In contrast, non-learning based denoising methods rely on imaging physics and mathematical constraints to construct explicit priors[15], enabling stable noise suppression without the need for extensive training datasets. Under low-dose CT conditions, a wide range of non-learning based

Received: 12 December 2025

Accepted: 21 February 2026

Published online: 25 March 2026

[1]School of Science, Shenzhen Campus of Sun Yat-sen University, Shenzhen 518107, China; [2]College of Information Science and Engineering, Northeastern University, Shenyang 110819, China; [3]School of Physics, Hefei University of Technology, Hefei 230009, China; [4]Beijing Synchrotron Radiation Facility, Institute of High Energy Physics, Beijing 100049, China; [5]Department of Ophthalmology, Yong Loo Lin School of Medicine, National University of Singapore, Singapore 117597, Singapore; [6]Guangzhou National Laboratory, No. 9 XingDaoHuanBei Road, Guangzhou International Bio Island, Guangzhou 510005, China.

*Correspondence: X Ge, E-mail: gexin5@mail.sysu.edu.cn

methods have been developed, including mean-based filters[16–20], sparse representation methods[21], prior-regularization frameworks such as total variation and its fractional-order extensions[22–25], non-local self-similarity approaches[26,27], and wavelet- or shearlet-based multi-scale transforms[28–31]. Moreover, various hybrid models that integrate transform-domain priors with learning-based components have been proposed[32–35]. These algorithms tend to enhance interpretability, providing potential advantages in clinical use.

In this work, we introduce a multi-Gaussian modeling strategy in the histogram domain. By generating a label map and optimizing their shapes, our method enables pixel-wise intensity adjustment for noise suppression. The generated label map yields a stable probability distribution, thereby ensuring consistent optimization results. The multi-Gaussian representation, with its multi-level gradient structure, better accommodates the heterogeneous density characteristics of biological tissues. Finally, variance reduction is applied to each Gaussian component according to assigned pixel labels. This not only produces images that more naturally resemble high-dose CT, but also inherently provides a form of material classification through the label assignment.

2 Results

2.1 High-fidelity denoising of zebrafish CT images

To evaluate the performance of mGCVR on biological samples, we first conducted experiments on a fixed zebrafish. A projection with an exposure time of 2.1 s was used as the ground truth, while the low-dose projection was acquired at 0.35 s, corresponding to a six-fold dose reduction. Figure 1(a) shows the raw, mGCVR-processed and ground truth images of the zebrafish body, where pseudo-color highlights the intensity distribution for a better comparison. Figure 1(b) and 1(c) present SSIM, RSP, and RSE obtained from a sliding-window analysis across the entire image, demonstrating consistent improvements at all spatial positions. Figure 1(d) presents a representative CT slice from the same zebrafish volume, and Fig. 1(e) shows the corresponding error maps before and after mGCVR processing. Figure 1(f–i) further evaluate the slice quality using MSE (mean squared error), PSNR (peak signal-to-noise ratio), SSIM (structural similarity index measure), RSE (resolution-scaled error), and RSP (resolution-scaled Pearson coefficient). As evaluated, mGCVR achieves substantial improvements in signal quality (PSNR), intensity fidelity (RSE), and structural similarity (RSP, SSIM) throughout the entire image.

2.2 Three-dimensional rendering of ant micro-CT images

To further demonstrate the effectiveness of mGCVR in recovering fine biological structures, Figure 2 presents both cross-sectional views and three-dimensional (3D) renderings of an ant specimen. Figure 2(a) shows a volumetric rendering of the ant from a dorsal view. Figure 2(b) magnifies the blue-boxed region in panel **a**, which corresponds to the compound eye and surrounding neural structures. mGCVR markedly reduces noise and restores the hexagonal structure of the compound eye cornea as well as the internal regular protrusions of retinula cells, consistent with the ground truth. Figure 2(c) enlarges the yellow-boxed region, located at the anterior thorax and neck. The cross-sections (top row) show improved micro-CT images of the inter segmental membranes, neural bundles, and internal air sacs after mGCVR processing. Figure 2(d) enlarges the green-boxed region along the lateral margin of the head capsule, here mGCVR improves the contrast of fine membranes and ensures sharper definition of tissue interfaces in both cross-section and volumetric renderings. Across all panels, mGCVR noticeably improves the contrast of micro-CT images, enhances features such as ommatidia and internal tissue boundaries, and produces 3D renderings with more coherent and continuous structures than in the noisy raw reconstructions.

2.3 Benchmark tests against established methods

We further validated mGCVR using the public dataset from the 2016 Low-dose CT AAPM Grand Challenge[36] and compared it with several classical denoising algorithms. Figure 3(a) shows a slice reconstructed from quarter-dose projections, with four regions of interest enlarged in Fig. 3(b–e). The red-box region in Figure 3 contains three hepatic lesions that are barely recognizable in the low-dose reconstruction. After mGCVR processing, the lesions become clearly identifiable, closely matching the full-dose reconstruction. The yellow-box region in Figure 3(c) shows fine structures in the lung, where mGCVR effectively suppresses noise without over-smoothing. The blue-box region in Figure 3(d), located around the stomach, further illustrates the noise-reduction capability of mGCVR in both air region and soft tissue. The green-box region in Figure 3(e) shows another hepatic lesion, where mGCVR enhances lesion conspicuity. Moreover, the mGCVR-processed images are free from the strong periodic artifacts commonly observed in self-similarity denoising methods. As summarized in Table 1, mGCVR achieves the highest SSIM among the compared methods and produces image quality close to that of high-dose CT. In addition, a detailed comparison between deep learning methods and mGCVR is presented in Supplementary Section 4. The results demonstrate that mGCVR outperforms RED-CNN and shows marginally better performance than TS-Net.

2.4 Mono-energetic-like contrast and tissue labeling

Another notable advantage of mGCVR is its ability to generate tissue labels directly from a wide-spectrum input. In

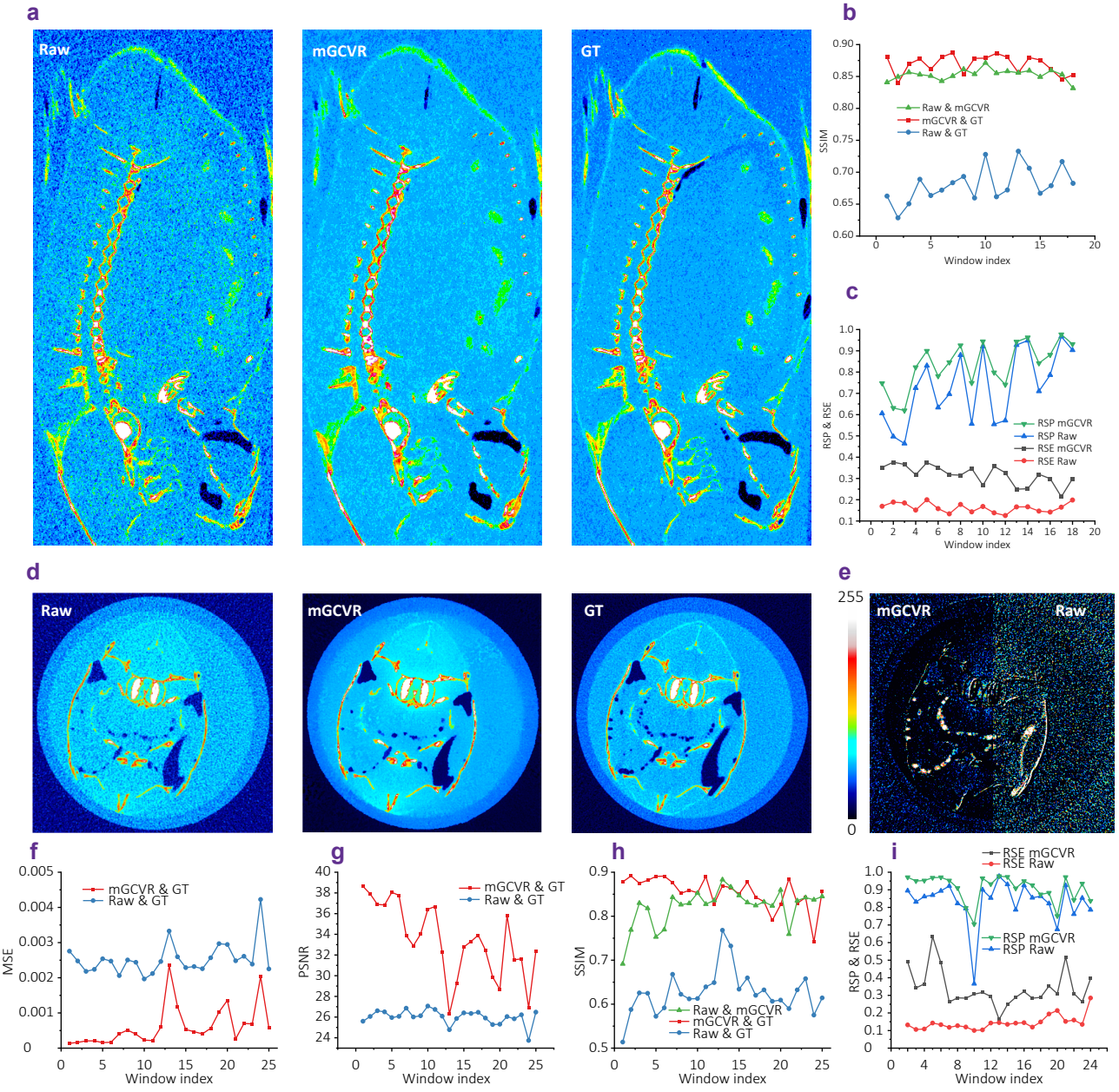

Fig. 1 | Zebrafish CT Image enhancement via mGCVR. (a) Cross-section orthogonal to the CT slice. From left to right: representative raw image, mGCVR-processed image, and ground truth. (b, c) Sliding-window analysis (window size: 100×100 pixels) performed on (a), with local SSIM, RSE, and RSP calculated within each window. (d) Representative CT slice from the same volume, shown as raw, mGCVR-processed and ground truth images. (e) Error maps of the slice in (d) comparing the mGCVR-processed image and the raw image with the ground truth. (f–i) Sliding-window analysis (window size: 64×64 pixels) performed on (d), with local MSE, PSNR, SSIM, RSE, and RSP calculated within each window.

Figure 4(a), the raw image is acquired at high energy (80 kVp) from the dual-energy CT challenge. Although acquired with a broad X-ray spectrum, mGCVR produces tissue-classification maps, such as adipose, fibroglandular, and calcified tissue. Results demonstrate that mGCVR-labels closely match with the ground truth labels obtained from a monoenergetic image. In Figure 4(b), we present a comparison between the ground truth obtained by threshold-based classification and the results produced by mGCVR. The classification performance is quantitatively evaluated using Accuracy, IoU, and Dice metrics (Figure 4(c)), demonstrating that mGCVR achieves an accuracy above 98%.

In Figure 4(d–g) (data from the 2016 Low-dose CT AAPM Grand Challenge), a small hepatic lesion is marked by white boxes. In the raw CT slice (Figure 4(e)), the lesion appears only as a faint dark shadow. After mGCVR processing, both the magnified 2D slices (Figure 4(f)) and the 3D renderings (Figure 4(g)) reveal the lesion with markedly

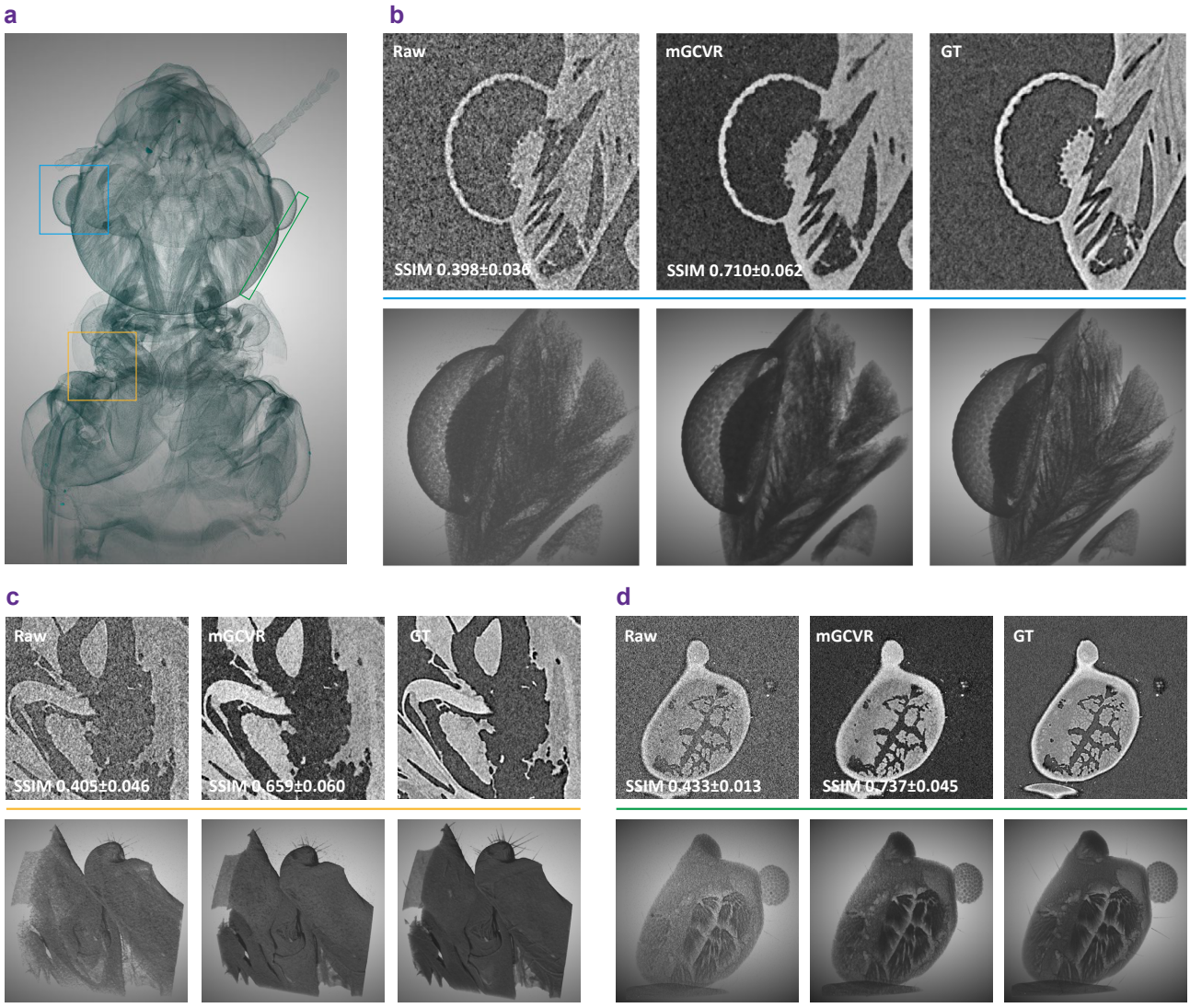

Fig. 2 | mGCVR enhances 3D ant visualizations. (a) Three-dimensional rendering of an ant specimen. Colored boxes indicate the regions enlarged in (b–d). (b) Magnified view of the compound eye and adjacent neural structures. (c) Magnified view of the anterior thorax and neck. (d) Magnified view of the lateral margin of the head capsule. SSIM values (mean ± standard deviation) are indicated below the CT slices.

improved contrast and morphological continuity. As shown in Figure 4(h), mGCVR further separates normal liver tissue from the lesion into different classes, demonstrating its capability for pathological tissue labeling.

3 Discussion

We further investigate the performance of mGCVR at an extremely low intensity level, simulated by reducing the intensity level (photon count) to 1/80 of the ground truth. As shown in Figure 5(a), mGCVR remains stable under severe noise and does not introduce noticeable artifacts. It is worth noting that the strong noise causes a substantial shift in the image mean, resulting in limited improvement in PSNR. In contrast, the SSIM value increases by more than a factor of four, indicating a significant enhancement in structural similarity.

In addition, quantitative assessment of clinical images demonstrate the consistent performance of mGCVR across different CT scanners (Figure 5(b)), noise levels (Figure 5(c)), and tissue characteristics. This stability arises from the algorithm's formulation based on the intrinsic statistical properties of CT data, which reduces sensitivity to scanner-specific or tissue-specific variations. Moreover, unlike many spatial-domain methods whose performance depends on fine parameter tuning, the main parameters in mGCVR exhibit stable and well-defined operating ranges. For the number of Gaussian components, six components are sufficient for effective denoising (Figure 5(d)). For standard 512×512 CT images, using six Gaussian components and a sliding-window size in the range of 32–56 pixels, could consistently achieve strong denoising performance (Figure 5(e)).

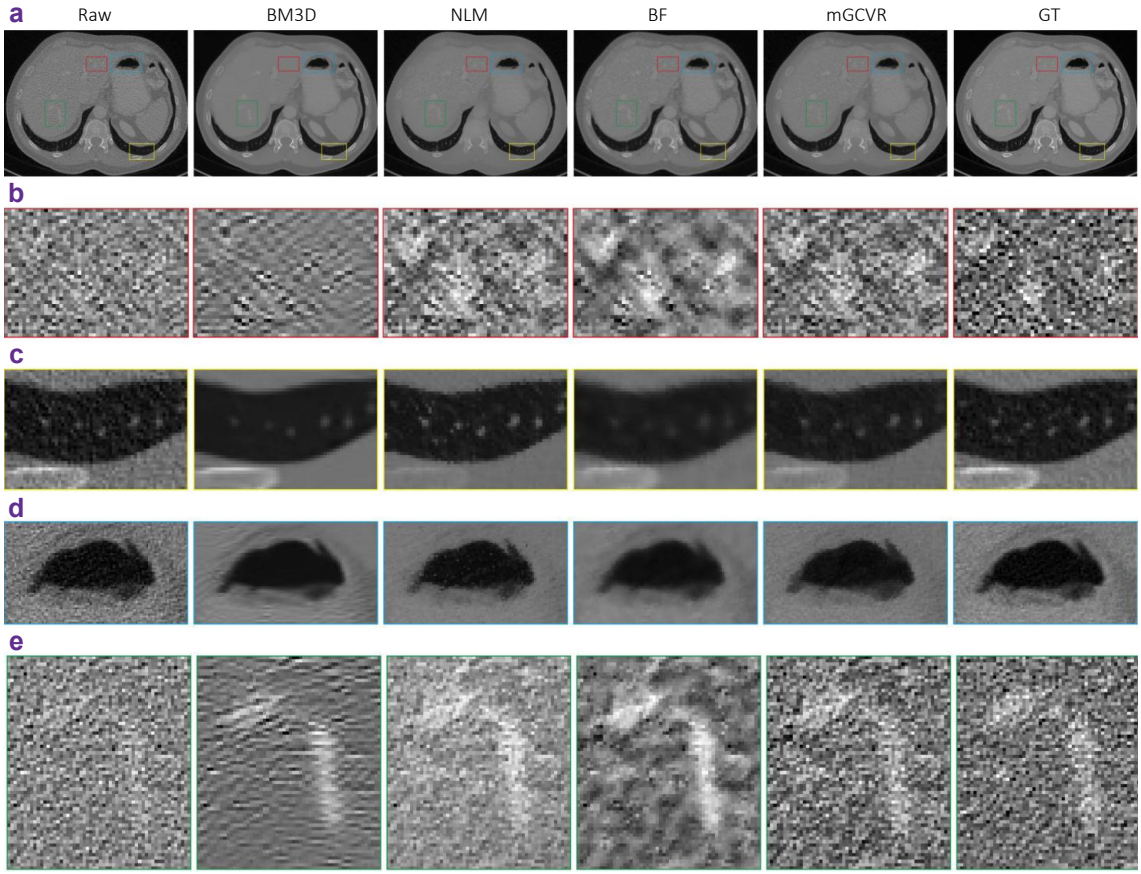

Fig. 3 | CT slice of the human abdomen. The Raw image is reconstructed from quarter-dose projections, while the GT image corresponds to the full-dose CT. Data are from the 2016 low-dose CT AAPM Grand Challenge[36]. (a) Overview of the full slice, regions marked by the colored boxes are magnified in (b–e). (b) Red box: three faint hepatic calcified lesions that are barely recognizable in the raw image. (c) Yellow box: partial view of the lung, where noise substantially obscures fine structures. (d) Blue box: region around the stomach, illustrating background reduction in both air region and soft tissue. (e) Green box: another calcified lesion.

Table 1 | SSIM values of different algorithms for the CT slice shown in Fig. 3.

Fig. 3	Raw	BM3D	NLM	BF	mGCVR
a	0.513	0.664	0.655	0.663	**0.673**
b	0.348	0.510	0.552	0.528	**0.552**
c	0.737	0.769	0.775	0.738	**0.795**
d	0.533	0.693	0.679	0.688	**0.697**
e	0.378	0.571	0.599	0.570	**0.600**

BM3D[37] automatically estimates the noise standard deviation to adjust the parameters. NLM[27] searches the parameter space to find the maximum SSIM. For BF[19] and mGCVR, the parameters are adjusted manually.

mGCVR introduces a fundamentally new method by formulating the difference between low-dose and high-dose CT as a statistical intensity classification problem. This formulation allows the method to accommodate diverse noise characteristics (Supplementary Section 1) and noise levels (Supplementary Section 2), thereby effectively improving CT image quality. This also brings several advantages. First, because mGCVR performs pixel-wise statistical inference, it inherently avoids localized or periodic artifacts. In contrast, nonlocal self-similarity methods often produce strong periodic patterns under extremely low SNR conditions. Pixel-wise processing enables mGCVR to generate images that closely resemble high-dose CT, rather than the over-smoothed results common in many conventional denoising methods. Second, mGCVR naturally preserves fine structural details. Classical averaging-based filters must balance noise suppression and edge preservation. In contrast, mGCVR conducts pixel labeling, and inter-label boundaries remain intrinsically sharp (Supplementary Section 6). Third, mGCVR is highly sensitive to intensity

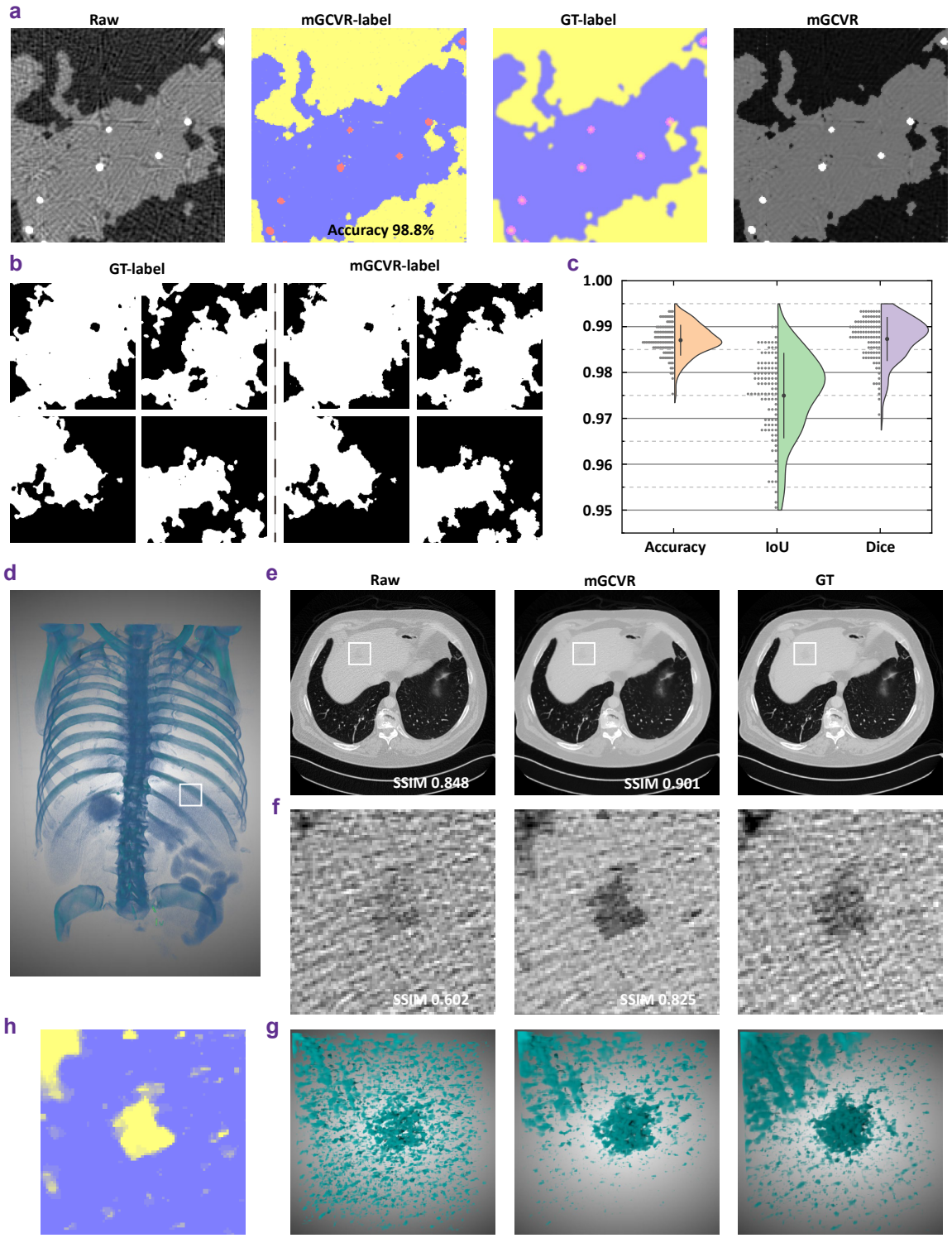

Fig. 4 | Tissue classification and pathological tissue labeling using mGCVR. The dataset in (a) is from the AAPM deep-learning spectral CT Grand Challenge[38]. The dataset in (b–f) is from the 2016 Low-dose CT AAPM Grand Challenge[36]. (a) Tissue classification results obtained from an 80 kVp wide-spectrum image (Raw) and the ground truth (GT), showing adipose (yellow), fibroglandular (blue), and calcified tissue (pink). (b) Representative results of basic threshold-based classification applied to the image labels in (a). (c) Half-violin plots of Accuracy, IoU, and Dice metrics over 100 images processed as in (b). (d) 3D rendering of the thoracic cavity. The white boxes indicate suspected liver-tumor tissues. (e) The CT slice corresponding to the white square in (d), where the lesion appears as dark shadows. (f) Magnified views of the boxed region in (d) and (e). (g) 3D renderings of the structures inside the boxed regions, showing recovered tumor morphology. (h) mGCVR-generated tissue-label map, illustrating clear separation between normal liver tissue (blue) and abnormal lesion tissue (yellow).

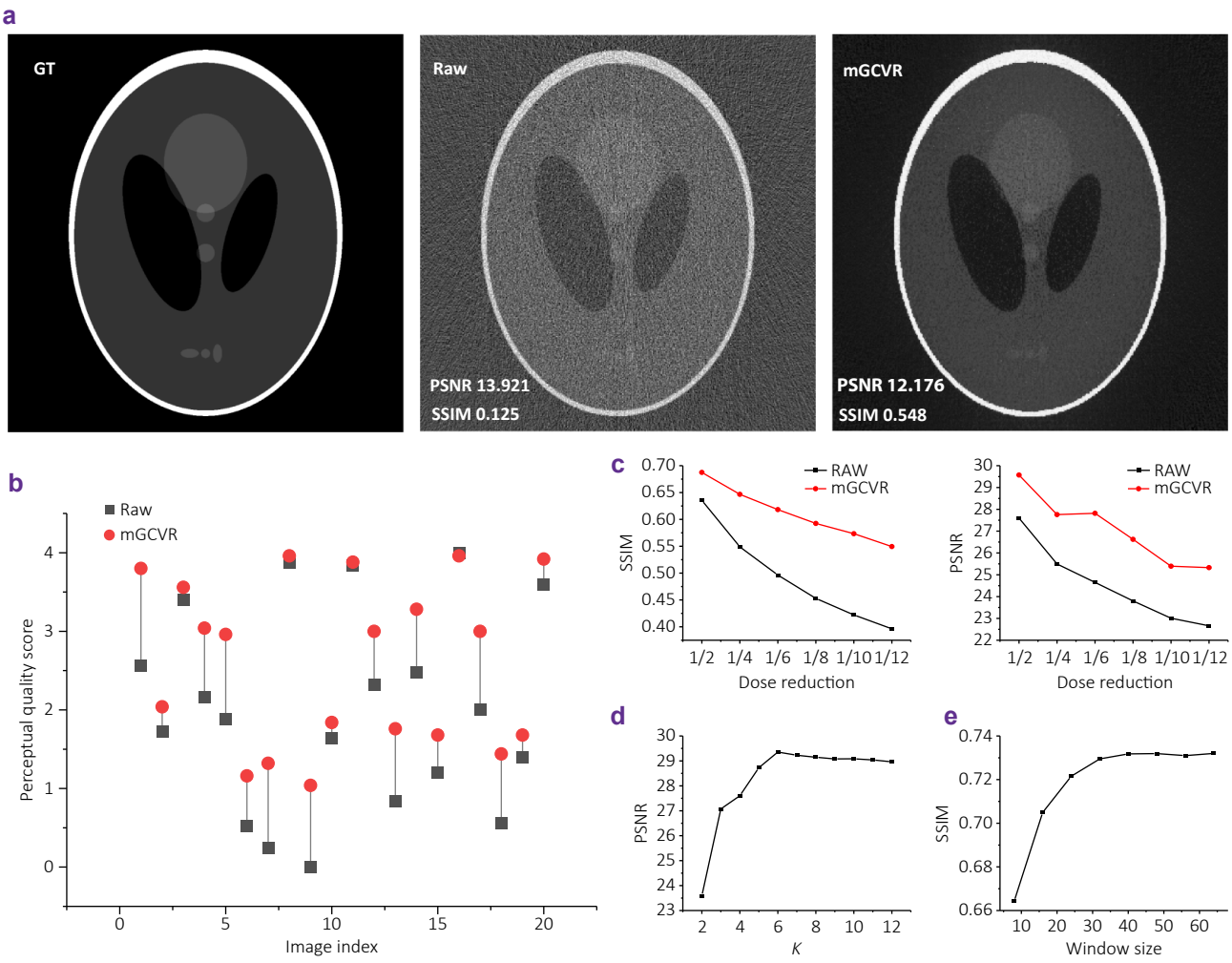

Fig. 5 | Robustness of mGCVR to noise and parameter settings. The dataset in (b) is from the MICCAI 2023 LDCT IQA[39]. The image quality assessment is performed using the Agaldran method. (a) Test on the Shepp-Logan phantom. From left to right: ground truth, simulated low-dose image, and mGCVR-processed image. (b) Quantitative assessment of 20 clinical images using the Agaldran method (scale 0–4, higher is better). The scatter plot compares the perceptual quality scores of raw LDCT images against mGCVR-processed images. (c) SSIM (left) and PSNR (right) as functions of dose reduction (1/2, 1/4, 1/6, 1/8, 1/10, and 1/12 of full dose) for clinical CT images processed with mGCVR. (d) Effect of the number of Gaussian components (K) on image quality measured by PSNR, with peaks at $K = 6$. (e) Relationship between sliding window size and corresponding SSIM.

variations, enabling improved discrimination of small attenuation differences between materials, which is beneficial for detecting early-stage pathological changes in medical imaging.

Despite these advantages, mGCVR also has limitations. Since pixel intensities are modeled by multi-Gaussian statistical fitting, its performance may degrade when the number of image pixels is small. For example, CT data acquired with large detector binning reduce the effective image pixels. In addition, if two materials exhibit very similar attenuation values and one of them is sparsely distributed, the Gaussian model may fail to separate the classes reliably. Furthermore, if two materials are mistakenly combined into a single Gaussian component, both will undergo identical variance suppression. In such cases, mGCVR may cause a minor contrast decrease rather than structural distortion. Importantly, this behavior is predictable and remains well controlled.

4 Conclusion

In this work, we proposed mGCVR, a novel histogram-domain framework for low-dose CT enhancement. Unlike conventional denoising methods that operate in the spatial or frequency domains, mGCVR performs statistical inference directly in the histogram domain by modeling the global intensity distribution with multiple Gaussian components and reducing intra-class variance. This formulation introduces a fundamentally different perspective on CT denoising, enabling noise suppression from a global statistical standpoint.

As a result, mGCVR inherently avoids the localized

artifacts commonly observed in spatial-domain or self-similarity-based methods, particularly under extremely low-dose conditions. By preserving the mean intensity of each component, the enhanced images maintain intensity distributions and visual characteristics that closely resemble high-dose CT.

In addition, the pixel-wise labeling mechanism allows simultaneous denoising and implicit tissue classification, improving sensitivity to subtle attenuation differences and enhancing the visibility of fine anatomical structures. Experimental results across biological and clinical datasets demonstrate that mGCVR consistently improves image quality and remains robust under extreme-low noise level.

As an interpretable computational method, mGCVR operates without data requirements and can be directly integrated into existing imaging workflows. Overall, this work establishes a histogram-domain paradigm for CT denoising and provides a practical yet powerful solution for reducing radiation dose while preserving image quality.

5 Method

5.1 mGCVR

In the mGCVR computation pipeline, the input image is processed using a sliding window, which extracts a sequence of overlapping square patches across the entire field of view with a fixed stride. For each patch, its intensity histogram is decomposed into multiple Gaussian components. As shown in Figure 6(a), three Gaussians (red, yellow, and blue) are used to fit the histogram in this example, although additional components may be required for heterogeneous tissues. Once the Gaussian decomposition and pixel-wise label map is obtained, noise suppression is achieved through pixel-wise intensity reassignment, in which each pixel intensity is adjusted to reduce the variance of its associated Gaussian-label component while preserving its mean (Figure 6(b)). All processed patches are then overlapped and recombined to form the final output image (Figure 6(c)). Figure 6(d) illustrates how pixel-wise labeling is achieved, and the detailed pseudocode is provided in Algorithm. 1. Notably, Gaussian fitting does not directly reduce noise. Noise suppression is achieved through the pixel-wise intensity reassignment in the final step.

Algorithm 1 mGCVR

Require: noisy CT image I; window size w;
number of Gaussian components K; maximum greedy iterations $N_{\max}$
Ensure: denoised image $\hat{I}$
1: divide image I into overlapping local patches P_i using a sliding window of size $w \times w$
2: **for** each patch P_i do
3: fit K-component 1D GMM to the intensity histogram of P_i
4: obtain Gaussian parameters $\{\mu_k, \sigma_k^2\}_{k=1}^{K}$
5: compute posterior probabilities $Pr(p \in k)$ for $k = 1, \ldots, K$

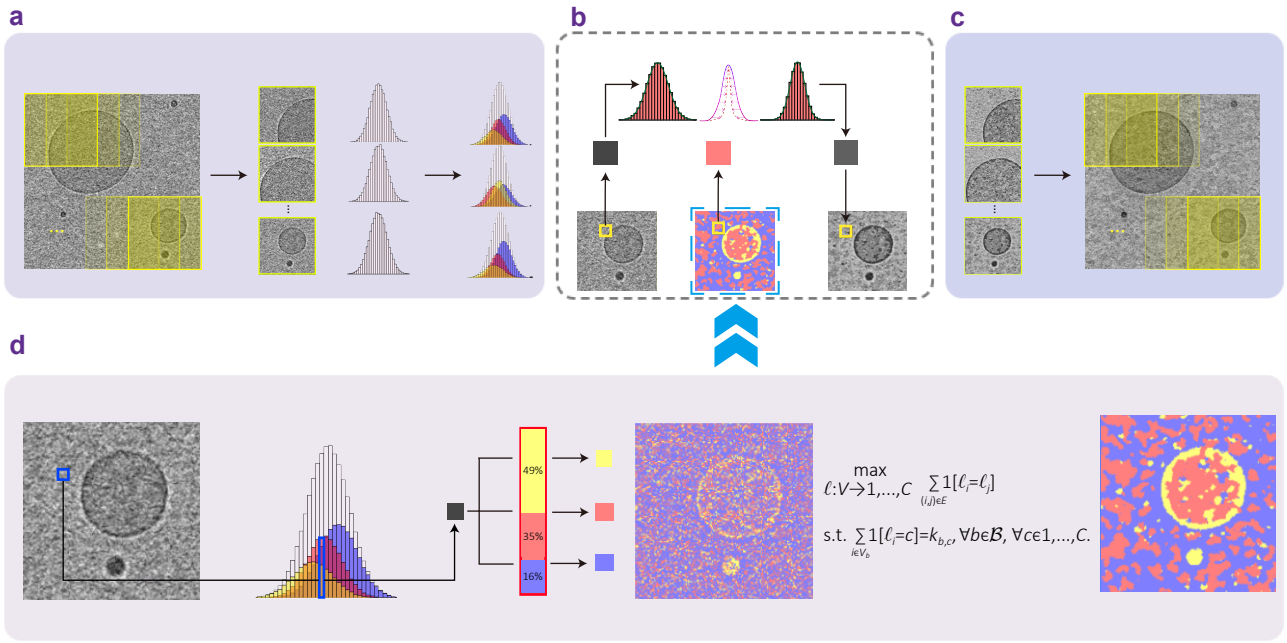

Fig. 6 | Workflow of the proposed mGCVR. (a) The input image is first divided into patches. For each patch, its intensity histogram is modeled using a multi-Gaussian fit. (b) Based on the fitted Gaussian components, each pixel is assigned a label, and the intensity distribution of each component is sharpened. (c) After variance reduction, all processed patches are stitched together to form the final output image. (d) Illustration of the labeling process for each patch, showing how pixels are classified into their corresponding Gaussian components.

6: sample label $l_p \sim \text{Categorical}(Pr(p \in 1), Pr(p \in 2), \ldots, Pr(p \in K))$
7: **repeat**
8: adjust label with Eq. (1)
9: **until** no improvement after $N_{\max}$ trials
10: **for** each pixel $\hat{x}_p$ do
11: shrink intensity toward its Gaussian mean

$$\hat{x}_p = \mu_k + \alpha\left(x_p - \mu_k\right), \quad 0 < \alpha < 1$$

12: **end for**
13: **end for**
14: aggregate all processed patches $\hat{P}_i$
15: **return** $\hat{I}$

Figure 6(d) illustrates the procedure used to generate the pixel-wise label map. First, each pixel in a patch is randomly assigned to one of the Gaussian components according to the component-wise probability derived from the histogram decomposition. This initial hard classification is then refined through an optimization step that encourages spatial clustering of pixels belonging to the same label. The optimization objective is defined as follows:

$$\max_{\ell:\, V\to 1,\ldots,C} \sum\nolimits_{(i,j)\in E} 1\left[\ell_i = \ell_j\right] \text{s.t.} \sum\nolimits_{i\in V_b} 1\left[\ell_i = c\right] = k_{b,c}\,, \quad \forall b \in \mathcal{B}, \forall c \in 1,\ldots,C. \tag{1}$$

Under the constraint that the number of pixels assigned to each label c within each intensity histogram bin b is fixed as $k_{b,c}$, we assign labels $l_i \in 1,\ldots,C$ are assigned to pixels so as to maximize the number of adjacent pixels sharing the same label. V denotes the set of all pixels, E is the set of adjacency pairs defined by the chosen neighborhood structure, $\mathbf{1}[l_i = l_j]$ is the indicator function (equal to 1 if $l_i = l_j$ and 0 otherwise), $\mathcal{B}$ is the set of intensity histogram bins, and $V_b \subseteq V$ is the set of pixels in bin b. The result of this constrained optimization yields the final label map, which is then used in the shrinkage step described in Figure 6(b).

5.2 Evaluation metric

To quantitatively demonstrate the effectiveness of the mGCVR algorithm, we used the metrics of RSE, RSP, SSIM, MSE, and PSNR for quantitative analysis. We define G as the reference image, M as the reconstructed image, N as the total number of pixels in the image, G_i, M_i as the gray-scale values of the i pixel, μ_G, μ_M as the image means, σ_G^2, σ_M^2 as the image variances, σ_{GM} as the image covariance, and L is the maximum gray level in the image.

To show the relative intensity error of the image, we use the RSE metric:

$$RSE = \frac{\sqrt{\sum_{i=1}^{N}\left(M_i - G_i\right)^2}}{\sqrt{\sum_{i=1}^{N} G_i^2}}\,. \tag{2}$$

To show the structural correlation of the image, we use the RSP metric:

$$RSP = \frac{\sum_{i=1}^{N}\left(M_i - \mu_M\right)\left(G_i - \mu_G\right)}{\sqrt{\sum_{i=1}^{N}\left(M_i - \mu_M\right)^2}\sqrt{\sum_{i=1}^{N}\left(G_i - \mu_G\right)^2}}\,, \tag{3}$$

here, RSE and RSP do not involve resolution changes. However, to be consistent with NanoJ-SQUIRREL[40], we still use the abbreviations RSE and RSP. To show the consistency of structure and contrast, we use the SSIM metric:

$$SSIM(M,G) = \frac{\left(2\mu_M\mu_G + C_1\right)\left(2\sigma_{MG} + C_2\right)}{\left(\mu_M^2 + \mu_G^2 + C_1\right)\left(\sigma_M^2 + \sigma_G^2 + C_2\right)}\,. \tag{4}$$

To show the average pixel error, we use the MSE metric:

$$MSE = \frac{1}{N}\sum_{i=1}^{N}\left(M_i - G_i\right)^2\,. \tag{5}$$

To show the error power, we use the PSNR metric:

$$PSNR = 10\log_{10}\left(\frac{L^2}{\frac{1}{N}\sum_{i=1}^{N}\left(M_i - G_i\right)^2}\right)\,. \tag{6}$$

To assess the accuracy of tissue recognition, we employ the metrics of Accuracy,

$$Accuracy = \frac{TP + TN}{TP + TN + FP + FN}\,. \tag{7}$$

Intersection over Union (IoU), and Dice similarity coefficient (Dice):

$$IoU = \frac{TP}{TP + FP + FN}\,, \tag{8}$$

$$Dice = \frac{2TP}{2TP + FP + FN}\,. \tag{9}$$

At the pixel level, a pixel is counted as a true positive (*TP*) if it is labeled in both the ground truth and the mGCVR result, a true negative (*TN*) if it is unlabeled in both, a false positive (*FP*) if it is unlabeled in the ground truth but labeled in mGCVR, and a false negative (*FN*) if it is labeled in the ground truth but unlabeled in mGCVR.

5.3 CT scanning parameters

To capture the microstructural features of various biological specimens and materials, we employed a laboratory micro-CT system to image zebrafish, ants, and AB adhesive samples. Imaging parameters including X-ray energy, magnification, and exposure time were selected according to specimen size and resolution requirements. For the zebrafish sample in Figure 1 *XY*-plane slices with a resolution of 35 μm were acquired at 60 kVp with 0.4× magnification. Paired reference and low-dose images were obtained using exposure times of 2.1 s and 0.35 s, respectively. The total photon count of the reduced-radiation images is approximately 1/6 of that of the full-dose ones. For the ant specimen in Figure

2 *XZ*-plane slices with a resolution of 2.5 μm were collected at 60 kVp and 4× magnification. The reduced-radiation images were acquired using an X-ray tube power of 1 W with an exposure time of 0.6 s, whereas the reference full-dose images were acquired at 6.51 W with an exposure time of 1 s. When both power and exposure time are taken into account, the total photon count of the reduced-radiation images is approximately 1/10.85 of that of the full-dose ones. For the AB adhesive sample in Figure 6 *XY*-plane slices with 1.25 μm resolution were acquired at 100 kVp and 4× magnification to characterize the cured microstructure. All datasets were reconstructed using the system's built-in algorithms and exported in TIFF format for subsequent analysis.

References

1. Withers PJ, Bouman C, Carmignato S et al. X-ray computed tomography. *Nat Rev Methods Primers* **1**, 18 (2021).
2. Mao YQ, Xu N, Wu YN et al. Assessments of lung nodules by an artificial intelligence chatbot using longitudinal CT images. *Cell Rep Med* **6**, 101988 (2025).
3. Marin D, Boll DT, Mileto A et al. State of the art: dual-energy CT of the abdomen. *Radiology* **271**, 327–342 (2014).
4. D'Angelo T, Cicero G, Mazziotti S et al. Dual energy computed tomography virtual monoenergetic imaging: technique and clinical applications. *Br J Radiol* **92**, 20180546 (2019).
5. Albrecht MH, Vogl TJ, Martin SS et al. Review of clinical applications for virtual monoenergetic dual-energy CT. *Radiology* **293**, 260–271 (2019).
6. Cong WX, Xi Y, Fitzgerald P et al. Virtual monoenergetic CT imaging via deep learning. *Patterns* **1**, 100128 (2020).
7. Yang YF, Wang HD, Liu ZY et al. Co-registration of OPM-MCG signals with CT using optical scanning. *iScience* **26**, 108235 (2023).
8. Fan Y, Zheng CY, Shu YF et al. Aberration-corrected differential phase contrast microscopy with annular illuminations. *Opto-Electron Sci* **4**, 240037 (2025).
9. Sadia RT, Chen J, Zhang J. CT image denoising methods for image quality improvement and radiation dose reduction. *J Appl Clin Med Phys* **25**, e14270 (2024).
10. Liao S, Mo ZH, Zeng MS et al. Fast and low-dose medical imaging generation empowered by hybrid deep-learning and iterative reconstruction. *Cell Rep Med* **4**, 101119 (2023).
11. Yu J, Zhang HT, Zhang P et al. Unsupervised learning-based dual-domain method for low-dose CT denoising. *Phys Med Biol* **68**, 185010 (2023).
12. Shan HM, Padole A, Homayounieh F et al. Competitive performance of a modularized deep neural network compared to commercial algorithms for low-dose CT image reconstruction. *Nat Mach Intell* **1**, 269–276 (2019).
13. Diwakar M, Pandey NK, Singh R et al. Low-dose COVID-19 CT image denoising using CNN and its method noise thresholding. *Curr Med Imaging* **19**, 182–193 (2023).
14. Katta S, Singh P, Garg D et al. A hybrid approach for CT image noise reduction combining method noise-CNN and shearlet transform. *Biomed Pharmacol J* **17**, 1875–1898 (2024).
15. Ge X, Chen S, Lin K et al. Deblurring, artifact-free optical coherence tomography with deconvolution-random phase modulation. *Opto-Electron Sci* **3**, 230020 (2024).
16. Kalra MK, Maher MM, Sahani DV et al. Low-dose CT of the abdomen: evaluation of image improvement with use of noise reduction filters-pilot study. *Radiology* **228**, 251–256 (2003).
17. Hilts M, Jirasek A. Adaptive mean filtering for noise reduction in CT polymer gel dosimetry. *Med Phys* **35**, 344–355 (2008).
18. Anam C, Haryanto F, Widita R et al. New noise reduction method for reducing CT scan dose: combining wiener filtering and edge detection algorithm. *AIP Conf Proc* **1677**, 040004 (2015).
19. Tomasi C, Manduchi R. Bilateral filtering for gray and color images. In *Sixth International Conference on Computer Vision (IEEE Cat. No. 98CH36271)* 839–846 (IEEE, 1998). https://doi.org/10.1109/ICCV.1998.710815.
20. Zhang M, Gunturk BK. Multiresolution bilateral filtering for image denoising. *IEEE Trans Image Process* **17**, 2324–2333 (2008).
21. Aharon M, Elad M, Bruckstein A. K-SVD: an algorithm for designing overcomplete dictionaries for sparse representation. *IEEE Trans Signal Process* **54**, 4311–4322 (2006).
22. Chowdhury MR, Zhang J, Qin J et al. Poisson image denoising based on fractional-order total variation. *Inverse Probl Imaging* **14**, 77–96 (2020).
23. Liu Y, Ma JH, Fan Y et al. Adaptive-weighted total variation minimization for sparse data toward low-dose x-ray computed tomography image reconstruction. *Phys Med Biol* **57**, 7923–7956 (2012).
24. Bredies K, Kunisch K, Pock T. Total generalized variation. *SIAM J Imaging Sci* **3**, 492–526 (2010).
25. Diwakar M, Singh P, Garg D. Edge-guided filtering based CT image denoising using fractional order total variation. *Biomed Signal Process Control* **92**, 106072 (2024).
26. Chen Y, Yang Z, Hu YN et al. Thoracic low-dose CT image processing using an artifact suppressed large-scale nonlocal means. *Phys Med Biol* **57**, 2667–2688 (2012).
27. Buades A, Coll B, Morel JM. Non-local means denoising. *Image Process Line* **1**, 208–212 (2011).
28. Zhang J, Liu GY, Chen JK et al. Multi-scale adaptive residual cold diffusion model for Low-Dose CT denoising. *Expert Syst Appl* **294**, 128817 (2025).
29. Starck JL, Candes EJ, Donoho DL. The curvelet transform for image denoising. *IEEE Trans Image Process* **11**, 670–684 (2002).
30. Diwakar M, Singh P. CT image denoising using multivariate model and its method noise thresholding in non-subsampled shearlet domain. *Biomed Signal Process Control* **57**, 101754 (2020).
31. Diwakar M, Singh P, Swarup C et al. Noise suppression and edge preservation for low-dose COVID-19 CT images using NLM and method noise thresholding in shearlet domain. *Diagnostics* **12**, 2766 (2022).
32. Danielyan A, Katkovnik V, Egiazarian K. BM3D frames and variational image deblurring. *IEEE Trans Image Process* **21**, 1715–1728 (2012).
33. Gu SH, Zhang L, Zuo WM et al. Weighted nuclear norm minimization with application to image denoising. In *Proceedings of the IEEE Conference on Computer Vision and Pattern Recognition* 2862–2869 (IEEE, 2014). https://doi.org/10.1109/CVPR.2014.366.
34. Dragomiretskiy K, Zosso D. Variational mode decomposition. *IEEE Trans Signal Process* **62**, 531–544 (2014).
35. Chen S, Lin K, Chen X et al. Spectrally extended line field optical coherence tomography angiography. *Opto-Electron Adv* **8**, 240293 (2025).
36. McCollough CH, Bartley AC, Carter RE et al. Low-dose CT for the detection and classification of metastatic liver lesions: results of the 2016 low dose CT grand challenge. *Med Phys* **44**, e339–e352 (2017).
37. Dabov K, Foi A, Katkovnik V et al. Image denoising by sparse 3-D transform-domain collaborative filtering. *IEEE Trans Image Process* **16**, 2080–2095 (2007).
38. Sidky EY, Pan XC. Report on the AAPM deep-learning spectral CT Grand Challenge. *Med Phys* **51**, 772–785 (2024).
39. Lee W, Wagner F, Galdran A et al. Low-dose computed tomography perceptual image quality assessment. *Med Image Anal* **99**, 103343 (2025).
40. Culley S, Albrecht D, Jacobs C et al. Quantitative mapping and mini-

mization of super-resolution optical imaging artifacts. *Nat Methods* **15**, 263–266 (2018).

Acknowledgements

This work was supported in part by Major Project of Guangzhou National Laboratory (GZNL2026A03001, GZNL2025C03014-01), Guangdong Basic and Applied Basic Research foundation (2023A1515011289), Guangdong Provincial Key Laboratory of Advanced Particle Detection Technology (2024B1212010005), Guangdong Provincial Key Laboratory of Gamma-Gamma Collider and Its Comprehensive Applications (2024KSYS001). We are grateful for the support provided by Mr. Bao Lu and Ms. Baoyun Shen of Carl Zeiss (Shanghai) Co., Ltd. We also thank the Instrumental Analysis & Research Center of SYSU (Zeiss Xradia 515 Versa) and Songshan Lake Materials Laboratory (Zeiss Xradia 610 Versa) for their assistance with X-ray imaging and technical services.

Author contributions

All authors commented on the manuscript.

Xiaofeng Zhang: Conceptualization, Methodology, Investigation, Data Curation, Formal Analysis, Visualization, and Writing-Original Draft; Yilan Zhu: Investigation, Formal Analysis, Visualization; Xin Ge: Conceptualization, Methodology, Formal Analysis, Supervision, Writing-Review & Editing, and Funding Acquisition; Linbo Liu: Funding Acquisition.

Competing interests

The authors declare no competing financial interests.

Supplementary information

Supplementary information for this paper is available at
https://doi.org/10.29026/oes.2026.250042